Reduction of Respiratory Motion Artifacts for Free-Breathing Whole-Heart Coronary MRA by Weighted Iterative Reconstruction

Christoph Forman[1,2], Davide Piccini [3,4], Robert Grimm[1], Jana Hutter[1,2], Joachim Hornegger[1,2], and Michael O. Zenge[5]

Affiliations:

1 Pattern Recognition Lab, Department of Computer Science, Friedrich-Alexander University of Erlangen-Nuremberg, Erlangen, Germany

2 Erlangen Graduate School in Advanced Optical Technologies (SAOT), Friedrich-Alexander University of Erlangen-Nuremberg, Erlangen, Germany

3 Advanced Clinical Imaging Technology, Siemens Healthcare H IM BM PI, Lausanne, Switzerland

4 Department of Radiology, University Hospital (CHUV) and University of Lausanne (UNIL) / Center for Biomedical Imaging (CIBM), Lausanne, Switzerland

5 MR Product Innovation & Definition, Healthcare Sector, Siemens AG, Erlangen, Germany

Notes:

Running Head: Weighted Iterative Reconstruction for Whole-heart CMRA

Correspondence to: Christoph Forman,
Pattern Recognition Lab
(Department of Computer Science)
Friedrich-Alexander University of Erlangen-Nuremberg,
Martensstr. 3, D-91058 Erlangen, Germany.
E-mail: christoph.forman@cs.fau.de.
Phone: +49 9131 85 27775
Fax: +49 9131 303811

Word count:

Abstract:	197	Figures:	8
Manuscript:	4998	References:	36

ABSTRACT

Purpose: To combine weighted iterative reconstruction with self-navigated free-breathing coronary MRA for retrospective reduction of respiratory motion artifacts.

Methods: 1D self-navigation was improved for robust respiratory motion detection and the consistency of the acquired data was estimated on the detected motion. Based on the data consistency, the data fidelity term of iterative reconstruction was weighted to reduce the effects of respiratory motion. In-vivo experiments were performed in 14 healthy volunteers and the resulting image quality of the proposed method was compared to a navigator-gated reference in terms of acquisition time, vessel length, and sharpness.

Result: Although the sampling pattern of the proposed method contained 60% more samples with respect to the reference, the scan efficiency was improved from $39.5 \pm 10.1\,\%$ to $55.1 \pm 9.1\,\%$. The improved self-navigation showed a high correlation to the standard navigator signal and the described weighting efficiently reduced respiratory motion artifacts. Overall, the average image quality of the proposed method was comparable to the navigator-gated reference.

Conclusion: Self-navigated coronary MRA was successfully combined with weighted iterative reconstruction to reduce the total acquisition time and efficiently suppress respiratory motion artifacts. The simplicity of the experimental setup and the promising image quality are encouraging towards future clinical evaluation.

Key words: Coronary MRA; Weighted iterative reconstruction, Motion suppression; Compressed sensing.

INTRODUCTION

Excellent soft tissue contrast combined with the absence of ionizing radiation draws magnetic resonance imaging (MRI) competitive to conventional computed tomography angiography for the diagnosis of the coronary arteries. For coronary magnetic resonance angiography (CMRA), an improved workflow has been provided with 3D whole-heart imaging [1, 2], which promises to extend the feasibility of coronary MRA also to more inexperienced operators.

The major drawback of whole-heart CMRA is the extended acquisition time, which renders the resulting images susceptible to artifacts due to any type of motion. Such artifacts originate from a reduced spatial consistency of the acquired data and typically appear as blurring or ghosting [3] in the images. Thus, compensation is required either during data acquisition or during image reconstruction in order to consistently achieve diagnostic image quality. In this context, cardiac motion is efficiently reduced by ECG-triggering and data acquisition during one of the cardiac resting phases, e.g. late systole and mid-diastole. This introduces a strong temporal restriction to the data acquisition window, as the late diastolic resting phase typically does not exceed 100 ms in the average cardiac patient population. As a consequence, a large number of heartbeats are required to complete the data acquisition. In free-breathing acquisitions, this prolongs the total acquisition time and increases the susceptibility of the data acquisition to respiratory motion. The latter is commonly addressed by prospectively gating the scan with a navigator to a small acceptance window in end-expiration [4, 5]. The major limitation of this method is that the acceptance rate of the navigator is often less than 50%, which negatively affects the total acquisition time. Irregularities in the breathing pattern [6] render this problem even worse and, more importantly, lead to an unpredictable scan time. To shorten scan times and to make a more efficient use of all acquired data, self-navigation has been proposed initially in combination with 3D radial imaging. In this approach, a k-space line is acquired at the beginning of every heartbeat with a superior-inferior (SI) orientation and used to detect and compensate for respiratory motion along this direction. The 1D Fourier transform of such line is referred to as SI projection. Because the detection of respiration by calculation of the center-of-mass [7] tends to underestimate the true motion of the heart, cross-correlation has been suggested for the tracking of the blood pool [8,9]. However, the robustness of such tracking methods is based on a reliable segmentation of the blood pool within the SI projections and can have a suboptimal performance in cases where the segmentation is uncertain [10]. Furthermore, the approximation of breathing motion as a 1D translation might not always be sufficient [11].

To overcome these shortcomings, a novel approach is proposed in the current work that aims to integrate and address the effects of respiratory motion in iterative image reconstruction. In particular, Johnson et al. [12] introduced the concept of weighted iterative reconstruction that generically accounts for data inconsistencies during a least squares optimization. To achieve this, the data fidelity term of the cost function is weighted relative to a data consistency measure. While, in the original work, data consistency was determined by a simple difference of k-space center samples, in the current work the data consistency measure is extracted from the respiratory displacement detected in the SI projections. Preliminary results of this method for coronary whole-heart imaging were shown in [13]. A similar approach based on the butterfly navigator has been successfully applied to reduce respiratory motion artifacts in free-breathing pediatric abdominal imaging [14]. In the current work, the respiratory motion detection method proposed in [9] has been extended to provide a more robust tracking. Furthermore, Johnson et al. already suggested that the image quality will greatly benefit from random sampling in combination with either parallel imaging [15,16] or compressed sensing [17]. Multiple ways to implement an incoherent sampling in the Cartesian phase-encoding plane were presented in recent publications [18–22]. Among these, the spiral phyllotaxis pattern [21] seemed to be particularly suitable for the current use case. In this work, an adapted version of the weighted iterative image reconstruction was implemented, which combines SI motion tracking and ℓ_1-regularized iterative SENSE reconstruction of sparse, incoherent input data. This was applied to free-breathing CMRA for the first time and was tested in 14 healthy volunteers in comparison to navigator-gated reference measurements.

METHODS

Free-breathing whole-heart CMRA is performed with interleaved acquisitions over many heartbeats. For the minimization of cardiac motion, data acquisition is triggered to the mid-diastolic resting phase. Henceforth, a set of readouts acquired within one heartbeat will be referred to as interleave. At the beginning of each interleave, one additional readout through the center of k-space is performed to obtain an SI projection. The information of the respiratory motion, extracted from the SI projections, is then utilized to estimate weighting factors to suppress respiratory motion artifacts during weighted iterative image reconstruction.

Binning into Respiratory Phases

The objective of the respiratory binning procedure, as already described in [22–24], is to robustly split the acquired data into subsets featuring minimum residual respiratory motion and high spatial consistency. In previous work [9], a contiguous group of pixels covering the signal of the blood pool in the SI projection was identified as a segment. Respiratory motion was detected by means of tracking this segment in subsequent SI projections. Instead of relying on the segmentation of the blood pool, in this work, multiple target segments with a fixed width of 20 pixels are analyzed in parallel. Then, one segment is identified that is most suitable to describe the respiratory pattern. This algorithm is illustrated in Figure 1 and can be described with the following two steps:

1. All SI projections are normalized relative to the maximum intensity of the first SI projection and sorted according to their time of acquisition as shown in Figure 1a. Let $\mathrm{SI}(t,x)$ describe the t-th SI projection out of a set of N_{SI} projections and x is the corresponding pixel position within the projection. Then, the signal variance over time is calculated for each pixel position by

$$\mathrm{var}_{\mathrm{temp}}(x) = \frac{1}{N_{\mathrm{SI}}} \sum_{t=1}^{N_{\mathrm{SI}}} \left(\mathrm{SI}(t,x) - \overline{\mathrm{SI}}_{\mathrm{temp}}(x)\right)^2, \tag{1}$$

where $\overline{\mathrm{SI}}_{\mathrm{temp}}(x)$ represents the mean signal intensity at x in the SI projections over time. Finally, multiple target segments for motion detection are defined in the first SI projection that fulfill two criteria: a) The center of a target segment is placed at a local maximum or minimum of the signal intensities in the first SI projection. b) In addition, a target segment must include a local maximum in $\mathrm{var}_{\mathrm{temp}}(x)$. While the first criterion ensures that the target segments cover the signal in the SI projection originating either from the center of an organ or a tissue boundary, the second guarantees that the target segment is subject to a significant degree of motion.

2. After the definition of multiple target segments in the first SI projection, respiratory motion is estimated for each segment in all subsequent SI projections using cross-correlation as described in [8,9]. Exemplarily, the detected offsets of two segments are plotted in Figure 1b. To identify the most reliable of all segments, the SI projections are then re-sorted according to the calculated offsets as illustrated in Figure 1c. After re-sorting, the local signal variation is measured similarly to the total variation norm [25] by the sum of finite differences of neighboring SI projections along the offset direction. The result with the smallest estimate corresponds to the target segment with the smoothest signal variation. Consequently, the associated segment is assumed to provide the best performance describing the respiratory pattern and is used for further processing.

Eventually, a binning is performed to split all imaging data into consistent subsets. While other approaches use the navigator [22, 23] or a manually selected part of the SI projection [24], the binning of the proposed method is based on the automatically chosen target segment from the previously described procedure. For all successive steps, the bin that contains the highest amount of spatially consistent data is chosen as reference. In the majority of cases, this bin corresponds to end-expiration [26]. While a high spatial consistency is expected within this reference, the consistency to the data of another bin decreases with an increasing respiratory offset.

Weighted Iterative Reconstruction

Similar as described in [13,14], the relation of data consistency and respiratory offset is exploited to reduce respiratory motion artifacts during weighted iterative reconstruction. In particular, readouts are weighted according to the respiratory distance of their corresponding bin to the reference using a scaled Gaussian kernel with the maximum set to 1 and centered on the reference bin. While [14] tune their weighting function to the maximum offset in end-expiration, the proposed method adjusts the weighting to the bin providing the largest amount of consistent data. In both methods, samples corresponding to respiratory phases close to the reference are weighted higher than those from distant phases during iterative reconstruction. However, samples from far distant bins are also weighted close to zero in this process, which renders the method equivalent to a retrospective soft-gating. The solution of the iterative reconstruction tends towards the reference respiratory phase and artifacts due to respiratory motion are inherently suppressed. The diagonal matrix $\mathbf{W}$ contains the estimated weights for each k-space sample, which is directly introduced into the data fidelity term of the cost function in iterative image reconstruction [12]:

$$f(\mathbf{x}) = \underset{\mathbf{x}}{\operatorname{argmin}} \|\mathbf{W}(\mathbf{A}\mathbf{x} - \mathbf{y})\|_2^2 + \lambda R(\mathbf{x}) \tag{2}$$

The first part of the cost function optimizes the data fidelity of the reconstructed volume, written as a concatenated vector $\mathbf{x} \in \mathbb{C}^{N_x N_y N_z}$ with respect to the measured data $\mathbf{y} \in \mathbb{C}^{N_k N_c}$, where N_k is the number of acquired k-space samples and N_c are the coil elements. $\mathbf{A} \in \mathbb{C}^{N_k N_c \times N_x N_y N_z}$ represents the MR system matrix including the receiver coil sensitivities, the Fourier transform and the sampling pattern. The second part represents the regularization term. In this work, regularization is realized using the total variation (TV) norm [25], which transforms the optimization problem into a compressed sensing reconstruction [17]. Equation 2 is solved using the limited-memory Broyden-Fletcher-Goldfarb-Shanno (L-BFGS) method [27].

MR Experiments

In-vivo experiments were performed in 14 healthy volunteers on a 1.5 T clinical MR scanner (MAGNETOM Aera, Siemens AG, Healthcare Sector, Erlangen, Germany), with software release syngo MR D13A. Signal reception was performed using an 18 channel body array coil and 8 elements of a spine array coil. Free-breathing whole-heart coronary MRA was performed in two successive experiments with sagittal slice orientation. Both 3D volume-selective, T2-prepared, fat-saturated bSSFP imaging sequences shared the following common parameters: TR/TE 4.0/2.0 ms, radio frequency excitation angle

90°, FOV $270 \times 270 \times 185\,\mathrm{mm}^3$, acquired matrix size $256 \times 218 \times 150$, reconstructed matrix size $256 \times 256 \times 176$, slice-oversampling 22%, voxel-size $1.05\,\mathrm{mm}^3$ and a receiver bandwidth of 849 Hz/Px. The sequence has been modified for use in this research study such that the Cartesian readouts are distributed in the phase-encoding plane on a spiral phyllotaxis arrangement similar to [21]. An additional SI projection was acquired at the beginning of each heartbeat, but was not used for image reconstruction. Prior to the imaging data, additional data was acquired in 21 heartbeats to fully sample the region in the center of k-space and to obtain coil sensitivity maps for image reconstruction.

For reference, respiratory motion was compensated by navigator gating in the first scan. An acceptance window of 5 mm was placed in end-expiration and slice tracking was set to a fixed correlation factor of 0.6 [26]. In this acquisition, the spiral phyllotaxis sampling pattern [21] was generated with 233 interleaves with 30 readouts. Including the obtained data for the coil sensitivity maps, this resulted in a moderate sub-sampling rate of 4.3 with respect to the fully sampled acquisition matrix.

In comparison to this, a second scan was performed with the proposed method. The setup of this acquisition was adjusted to achieve equivalent conditions to the reference during image reconstruction. For this purpose, the standard deviation of the Gaussian for the weighting kernel was set to 1.25 pixels to obtain a similar width to the 5 mm navigator acceptance window. In this setup, only the samples with a corresponding weight greater than 0.05 noticeably contribute to the reconstruction of the final image. Hence, solely those samples were considered for the calculation of the effective net acceleration in reconstruction relative to the size of the acquisition matrix in the phase-encoding plane. Even in the presence of a retrospective soft-gating by the weighting procedure, the incoherent sampling within one heartbeat and a golden angle rotation between the readouts of consecutive heartbeats of the spiral phyllotaxis pattern makes the reacquisition of data unnecessary to preserve a uniformly covered k-space. However, this retrospective sub-sampling of k-space during reconstruction must be compensated during data acquisition by an increased number of interleaves in order to facilitate a comparable sub-sampling rate to the reference. Prior experiments established that this can be accomplished by setting the number of interleaves to the next Fibonacci number, i.e. 377, which provides also an equivalent sampling of the readouts within each heartbeat at the same time. Although respiratory gating was deactivated for this scan, the navigator signal was still acquired to perform an offline correlation with the outcome of the motion detection based on the SI projections.

All data was reconstructed with the described iterative reconstruction, but different settings were applied: First, retrospective soft- and hard-gating were compared. For this purpose, the acquired data of the second scan were reconstructed with weighting kernels featuring different acceptance windows that were obtained from Gaussian and box functions. In retrospective hard-gating, the width of the box function was set to A) ± 2.5 pixels, B) ± 5.5 pixels, and C) ± 7.5 pixels. A similar setup in soft-gating was achieved by setting the Gaussian to 1.25 pixels in case of A). For B) and C), the Gaussian was adapted such that it intersects the corresponding box function at the same value, which was achieved by 2.75 pixels and 3.75 pixels for the standard deviation, respectively. For each subject, the weighting kernels were centered to the identical respiratory reference phase. Iterative reconstruction was performed without regularization, i.e. $\lambda = 0$, and the optimization was terminated after a fixed number of 8 iterations. Thereafter, data of the navigator-gated acquisition were reconstructed for comparison to the proposed method. For this purpose, $\mathbf{W}$ was set to the identity matrix, which deactivated the weighting procedure. The data of the second scan were reconstructed twice: first without weighting to demonstrate the effect of motion in the data and then with soft-gating using kernel A) towards end-expiration. For this comparison, iterative reconstruction was performed with a fixed regularization parameter $\lambda = 2 \cdot 10^{-5}$ was terminated after a fixed number of 8 iterations.

Data obtained for the estimation of the coil sensitivity maps were also included in image reconstruction. Therefore, a book-keeping was integrated into image reconstruction to manage redundant readouts. While duplicate readouts replaced previously acquired data when the weighting was deactivated, readouts with the closest distance to the respiratory reference phase were selected otherwise. Both respiratory motion detection and compressed sensing image reconstruction were fully integrated into the software of the MR scanner.

Data Analysis

The average acquisition time of the proposed method was compared to the navigator-gated reference scan in order to assess the scan efficiency. For evaluation of the respiratory motion detection, the offsets detected in SI projections were correlated to the outcome of the simultaneously acquired navigator signal. The slope of the linear regression between the feedback of the navigator and the proposed motion detection was computed. Furthermore, the automated selection of the target segment in the SI projection was evaluated by comparing it to the corresponding anatomy in the field of view of the imaging volume. For this purpose, the region of the segment in a SI projection of the reference bin was matched to the reconstructed volume. During all reconstructions, the residual error of the data fidelity term was recorded. The difference of the estimated image to the measured data at the final iteration was used for comparison of the different reconstruction methods. As the deviation of the estimated image and the acquired data is expected to be minimal and close to the noise level in the optimal case and increases in the presence of data inconsistencies. This measure provides an indication on the existing data consistency. However, this value is biased by the underlying signal intensities and scales with the number of considered samples. Therefore, it was normalized by $\|\mathbf{W}\mathbf{y}\|_2^2$ for the evaluation in each case, which is equivalent to the difference of the measured data to a zero image $\mathbf{x} = \mathbf{0}$ at the initialization of the iterative reconstruction. For quantitative assessment of the influence of different weighting kernels on the resulting image quality, vessel sharpness was evaluated in the reconstructed images. In particular, a centerline in the right coronary artery (RCA) and left anterior descending (LAD) was manually segmented in the 3D isotropic volume using CoronaViz (Work in progress software, Siemens Corporate Research, Princeton, NJ, USA). Within the first 40 mm of each centerline, five points were selected in the volumes that were at consistent positions for each volunteer. At each measurement point, a cross-section was sampled perpendicular to the centerline. On this cross-section the sharpness was evaluated as described in [28]. Finally, vessel sharpness for each coronary vessel was estimated by averaging the results of all cross-sections. In the comparison study to the navigator reference, the length of the segmented centerline was additionally measured. Furthermore, image quality was qualitatively assessed by two independent observers (M.O.Z and C.F.) with more than 8 and 3 years experience in the field of cardiovascular MRI, respectively. Visual scores were given to rate the delineation of the RCA and LAD following the study design described in [22] with a five-point scale: 0, no; 1, poor; 2, fair; 3, good; and 4, excellent. A paired two-tailed Student's t-test was performed in all obtained results to evaluate statistical significance. P-values of 0.05 or less were considered as statistically significant.

RESULTS

All whole-heart free-breathing acquisitions were successfully completed in all volunteers. The average navigator acceptance rate was $39.5 \pm 10.1\%$, which resulted in a total acquisition time in the range of 6.6 min to 20.2 min and required 10.1 ± 2.3 min, on average. Although 144 more interleaves were used for the sampling pattern of the proposed method compared to the reference scan, acquisition time was reduced to 6.3 ± 0.9 min. This reduction of scan time is statistically significant ($P < 0.001$). Since the proposed method is only dependent on the subject's heart rate, the range of the acquisition times was reduced to 5.0 min and 7.4 min.

When correlating the target segments which were selected for motion detection by the proposed algorithm with the anatomy of the volunteers, it turned out that such segments were always automatically defined near the position of the diaphragm. Representatively, Figure 8 shows a series of 50 consecutive heartbeats that were acquired in the experiment with one of the subjects. In this plot, the defined interval is highlighted with a red line that also outlines the detected effect of respiratory motion. Re-sorting these SI projections according to the estimated offsets enables a visual assessment of the efficacy of the proposed approach. Generally, the detected offsets had an average correlation to the simultaneously acquired navigator signal of 0.92 ± 0.06. For the same subject, Figure 3 illustrates in a joint histogram that the feedback of the proposed method is in full accordance with the feedback from the navigator. This observation is quantitatively confirmed for all volunteers by an almost unitary average slope of the linear regression: 0.96 ± 0.22.

The comparison of different weighting kernels is exemplarily shown in Figure 4 for the RCA of one subject and all quantitative results are summarized in Figure 5 Increasing the standard deviation of the Gaussian kernel for soft-gating only slightly reduced the vessel sharpness of the RCA, which was measured with $0.408 \pm 0.036\,\mathrm{mm}^{-1}$ for kernel A), $0.399 \pm 0.039\,\mathrm{mm}^{-1}$ for kernel B), and $0.389 \pm 0.034\,\mathrm{mm}^{-1}$ for kernel C). A similar trend was observed for the measurements in the LAD with $0.367 \pm 0.029\,\mathrm{mm}^{-1}$, $0.352 \pm 0.037\,\mathrm{mm}^{-1}$, and $0.343 \pm 0.041\,\mathrm{mm}^{-1}$, respectively. This effect is enhanced when increasing the acceptance window during hard-gating: $0.403 \pm 0.036\,\mathrm{mm}^{-1}$, $0.382 \pm 0.034\,\mathrm{mm}^{-1}$, and $0.361 \pm 0.034\,\mathrm{mm}^{-1}$ for the RCA and $0.358 \pm 0.029\,\mathrm{mm}^{-1}$, $0.340 \pm 0.037\,\mathrm{mm}^{-1}$, and $0.311 \pm 0.032\,\mathrm{mm}^{-1}$ for the LAD.

For each volunteer, the data of 219.1 ± 36.3 heartbeats were weighted greater than 0.05. After the retrospective soft-gating, this corresponds to a net acceleration of 5.1 ± 0.9 relative to the fully sampled k-space. This implies that the amount of consistent data was on average lower than in the navigator-gated reference scan featuring a net acceleration of 4.3. n all cases, the improvement of the data fidelity in the last iteration was less than 0.1 % relative to the ℓ_2-norm of the acquired data, which confirms convergence of the optimization. Without compensation, motion-induced inconsistency leads, after 8 iterations, to a data fidelity as low as 0.14 ± 0.04. Considering the estimated weights in the proposed method, this normalized difference converged to 0.06 ± 0.02, which means a significant improvement ($P < 0.001$). However, prospective navigator gating of the data acquisition resulted in the lowest value of the data fidelity term with 0.04 ± 0.01 ($P < 0.02$). For two selected volunteers, Figure 6 shows the reformatted images of the RCA and LAD for a side-by-side comparison. The quantitative results are summarized in Figure 7. As expected, volumes reconstructed without respiratory motion compensation were corrupted by artifacts. Hence, a reduced visible vessel length of 68.5 ± 20.0 mm for the RCA and 54.9 ± 38.0 mm for the LAD were observed in these volumes. The evaluation of vessel sharpness resulted in $0.381 \pm 0.047\,\mathrm{mm}^{-1}$ and $0.328 \pm 0.051\,\mathrm{mm}^{-1}$, respectively. The resulting image quality was rated by the observers with 1.3 ± 0.8 for the RCA and 1.0 ± 0.8 for the LAD. Using the proposed weighted reconstruction, both the perceived and the quantitative image quality was improved. This enabled a continuous detection of the coronary vessels over a significantly increased length ($P < 0.01$): i.e. 101.6 ± 18.9 mm for the RCA and 99.7 ± 15.7 mm for the LAD. The evaluation of vessel sharpness along the segmented centerlines followed the same trend with $0.426 \pm 0.057\,\mathrm{mm}^{-1}$ and

$0.384 \pm 0.045\,\text{mm}^{-1}$ ($P < 0.001$). This significant improvement ($P < 0.001$) was also measured in the visual scores with 2.8 ± 0.8 and 2.5 ± 0.7, respectively. The navigator-gated reference volumes showed a slightly superior vessel length with $108.6 \pm 15.7\,\text{mm}$ (RCA) and $109.6 \pm 20.2\,\text{mm}$ (LAD) as well as vessel sharpness $0.449 \pm 0.051\,\text{mm}^{-1}$ and $0.401 \pm 0.043\,\text{mm}^{-1}$, respectively. Compared to the results of the navigator-gated reference acquisition, an equivalent vessel length was detected in the volumes obtained with the proposed method ($P > 0.32$). While vessel sharpness of the RCA followed the same trend ($p > 0.1$), still a significant difference was found for the LAD ($P < 0.01$). The visual scores confirmed this observation with 3.0 ± 0.9 for the RCA ($P > 0.59$) and 3.1 ± 0.7 for the LAD ($P < 0.01$).

Figure 8 shows the reconstructed images of two volunteers to assess the influence of the breathing pattern on the resulting image quality. The histograms illustrate the distribution of the respiratory offsets as detected in the SI projections during the scan. Both volumes were reconstructed with a similar amount of data that were weighted greater than 0.05. However, the distribution of the data in the histogram is different. In the first dataset, end-expiration was consistently in the same respiratory phase throughout the entire scan, which lead to a reference respiratory phase containing roughly one third of all available data. The weighted reconstruction of this dataset has a comparable image quality to the navigator-gated reference. In the second dataset, the end-expiratory phase drifted in the middle of the scan and only 18% of the data fell into the reference phase. While the respiratory phase corresponding to the detected offset 0 represents the most consistent phase in end-expiration, the data of the remaining heartbeats is approximately uniformly distributed over the detected respiratory phases resulting in residual artifacts after weighted reconstruction.

DISCUSSION

One of the advantages of self-navigated coronary MRA is that the total scan time is predictable. This potentially allows to integrate coronary imaging into an existing cardiac routine examination, similarly as done in the first patient study on self-navigation described in [29]. In the current study, it was demonstrated that the total acquisition was approximately two times faster with weighted iterative reconstruction although 60%

more data were acquired compared to a navigator gated reference scan. As the objective of this study was to examine the reduction of motion artifacts during iterative reconstruction, a moderate net acceleration was chosen for data acquisition. More advanced regularization techniques, that e.g. incorporate spatial similarities learned from the images during reconstruction [30], promise to be superior to the presented TV regularization and might also allow the reconstruction at an increased sub-sampling rate. Such methods can be combined with weighted iterative reconstruction, which might enable a further acceleration.

In this work, it was proven that reliable motion detection is possible without prior knowledge of the object and without the need for manual user interaction. Respiratory motion detection was successfully able to define a segment in the SI projection that reliably describes the respiratory motion pattern in all the volunteers. Automatic selection of this segment renders the entire method independent of the position of the field of view chosen for imaging. Although this detection method is not limited to a sagittal slice orientation, it clearly benefits from readouts acquired along the predominant direction of respiratory motion. Generically, the proposed algorithm aims to detect signal variations in the intensities that describe the motion pattern during the data acquisition. This provides the potential for other applications also in other regions in the abdomen or with different imaging contrasts.

Segments used for motion detection were always automatically defined in the SI projections at locations that coincide with the position of the diaphragm within the selected field of view. With the current acquisition protocol, the high contrast between the lung and the liver favors an easy detection of motion in the SI projection. Additionally, this region is also most prominently subject to respiratory motion [26]. Since the diaphragm also provides the basis for the navigator signal, this is a highly probable explanation for the high correlation with the proposed respiratory motion detection. Moreover, the almost unitary slope of the linear regression implies that the detected offsets of both methods are nearly identical. Thus, the signal of a navigator monitoring the diaphragmatic position could alternatively be used as input for the described weighted iterative reconstruction. However, this would require a higher expertise of the operator and come with the price of an additional expenditure for its setup during the planning of the examination. Similarly to the navigator, segment locations near the diaphragm might render the proposed method prone to respiratory hysteresis. As a consequence, this would negatively affect the linear model between the diaphragm and the heart motion and possibly lead to incorrect estimated weights for the data consistency. The hysteretic loops [6] describing the respiratory hysteresis suggest that the impact of this effect can be reduced by the discrimination between inspiration and expiration. Hence, taking the temporal information of the SI projections into account for the binning process could potentially provide a solution for this problem. Furthermore, as observed in [6] the hysteretic loops show a minimum deviation from the linear model linking the heart and diaphragmatic motion between end-expiration and inspiration. Typically, the proposed weighting is maximum for this particular phase and respiratory phases that are subject to an increasing impact of respiratory hysteresis are weighted less during the iterative reconstruction or are even not considered. Since none of the performed in-vivo experiments of this study showed noticeable hysteresis effects, its influence on weighted reconstruction still needs to be investigated.

As expected, motion-induced data inconsistency leads to a degraded image quality in the reconstructed images, which is also reflected in a high residual difference of the data fidelity term and low image quality scores. Weighting the data during iterative reconstruction efficiently preserves the data consistency, which was confirmed by a data fidelity that is evolving towards the navigator-gated reference. Low differences between hard- and soft-gating in case of kernel A) can be explained with a low motion-induced data inconsistency for respiratory phases close to the reference. However, as the data inconsistency increases with the size of the acceptance window, this decreased the vessel sharpness in hard-gating. While the iterative reconstruction is biased towards one consistent respiratory phase during soft-gating, effects of respiratory motion are suppressed independently of the direction of motion even in the presence of large acceptance windows. Effects of respiratory motion in any direction that increase linearly with the respiratory offset relative to the reference phase are likewise suppressed during weighted iterative reconstruction. This also becomes evident in the scores evaluating the image quality in the reconstructed images that are in a comparable range to the outcome of the navigator acquisition.

The major limitation of the proposed method is that retrospective soft-gating leads to a further reduction of the available data for image reconstruction. In this context, the distribution of the acquired data in the different respiratory phases also seems to have an effect on the resulting image quality. The proposed method is still coupled with the subject's breathing pattern during data acquisition. In some cases, this combination of residual motion and an increased sub-sampling might lead to artifacts that still impair the image quality in the reconstructed volumes. This might be particularly the case when the breathing pattern changes frequently during the scan. In this study, weighting of the data fidelity term led to an increased sub-sampling compared to data available for reconstruction of the navigator-gated reference acquisition. Potentially, this explains the slightly inferior image quality scores and the remaining significant difference in vessel sharpness of the LAD between the proposed method and the reference.

The incorporation of data from all respiratory phases might allow to overcome these limitations. This requires an integration of a 3D non-rigid motion model similarly as proposed by [22,31,32]. In order to avoid the need for extra calibration data [33], effects of respiratory motion might also be visualized utilizing multiple iterative reconstructions weighted to different respiratory phases. Accepting longer processing times due to the demanding computational complexity, such methods promise to reduce artifacts originating from an increased sub-sampling. Alternatively, individual respiratory phases can be seen as a temporal component. Thus, equivalent as proposed for k-t SPARSE [34] or low-rank methods [35,36], the redundancy in these volumes could be exploited by a compressed sensing reconstruction to obtain the final image without the need to explicitly estimate a motion model.

CONCLUSION

In the current work, weighted iterative reconstruction was first applied to whole-heart coronary imaging and was successfully combined with self-navigation which allowed to significantly reduce the total data acquisition time. The improved motion detection algorithm together with the highly predictable scan time advocates this method for further testing in patients. In some cases, however, the current solution remains a tradeoff between increased sub-sampling artifacts or residual motion artifacts. Nevertheless, these promising initial results and the consequent integration of the current prototype solution into a clinical MR scanner is appealing for more extensive studies in volunteers and patients.

ACKNOWLEDGMENTS

The authors gratefully acknowledge funding of the Erlangen Graduate School in Advanced Optical Technologies (SAOT) by the German Research Foundation (DFG) in the framework of the German excellence initiative.

REFERENCES

[1] Weber Oliver M, Martin Alastair J, Higgins Charles B. Whole-Heart Steady-State Free Precession Coronary Artery Magnetic Resonance Angiography. Magnetic Resonance in Medicine 2003;50:1223–1228.

[2] Hauser Thomas H, Manning Warren J. The Promise of Whole-Heart Coronary MRI. Current Cardiology Reports 2008;10:46–50.

[3] Wood Michael L, Henkelman R Mark. MR image artifacts from periodic motion. Medical Physics 1985;12:143.

[4] Danias P G, McConnell M V, Khasgiwala V C, Chuang M L, Edelman R R, Manning W J. Prospective Navigator Correction of Image Position for Coronary MR Angiography. Radiology 1997;203:733–736.

[5] Stuber M, Botnar R M, Danias P G, Kissinger K V, Manning W J. Submillimeter Three-dimensional Coronary MR Angiography with Real-time Navigator Correction: Comparison of Navigator Locations. Radiology 1999;212:579–587.

[6] Nehrke K, Börnert P, Manke D, Bock J C. Free-breathing Cardiac MR Imaging: Study of Implications of Respiratory Motion–Initial Results. Radiology 2001;220:810–815.

[7] Stehning C, Börnert P, Nehrke K, Eggers H, Stuber M. Free-Breathing Whole-Heart Coronary MRA with 3D Radial SSFP and Self-Navigated Image Reconstruction. Magnetic Resonance in Medicine 2005;54:476–480.

[8] Lai Peng, Larson Andrew C, Bi Xiaoming, Jerecic Renate, Li Debiao. A Dual-Projection Respiratory Self-Gating Technique for Whole-Heart Coronary MRA. Journal of Magnetic Resonance Imaging 2008;28:612–620.

[9] Piccini Davide, Littmann Arne, Nielles-Vallespin Sonia, Zenge Michael O. Respiratory Self-Navigation for Whole-Heart Bright-Blood Coronary MRI: Methods for Robust Isolation and Automatic Segmentation of the Blood Pool. Magnetic Resonance in Medicine 2012;68:571–579.

[10] Piccini Davide, Bonanno Gabriele, Ginami Giulia, Littmann Arne, Zenge Michael O, Stuber Matthias. Optimized Respiratory Reference Position for 3D Self-Navigated Whole Heart Coronary MRA. In: Proceedings of the 21st Annual Meeting of ISMRM, Salt Lake City, UT, USA; 2013. p 1316.

[11] Nehrke Kay, Börnert Peter. Prospective Correction of Affine Motion for Arbitrary MR Sequences on a Clinical Scanner. Magnetic Resonance in Medicine 2005;54:1130–1138.

[12] Johnson Kevin M, Block Walter F, Reeder Scott B, Samsonov Alexey. Improved Least Squares MR Image Reconstruction Using Estimates of k-space Data Consistency. Magnetic Resonance in Medicine 2012;67:1600–1608.

[13] Forman C, Piccini D, Hutter J, Grimm R, Hornegger J, Zenge M O. Minimization of Respiratory Motion Artifacts for Whole-Heart Coronary MRI: A Combination of Self-navigation and Weighted Compressed Sensing Reconstruction. In: Proceedings of the 20th Annual Meeting of ISMRM, ; 2012. p 1160.

[14] Zhang Tao, Cheng Joseph Y, Potnick Aaron G, Barth Richard A, Alley Marcus T, Uecker Martin, Lustig Michael, Pauly John M, Vasanawala Shreyas S. Fast pediatric 3D free-breathing abdominal dynamic contrast enhanced MRI with high spatiotemporal resolution. Journal of Magnetic Resonance Imaging 2013, doi: 10.1002/jmri.24551.

[15] Pruessmann K.P., Weiger M, Scheidegger M B, Boesiger P. SENSE: Sensitivity Encoding for Fast MRI. Magnetic Resonance in Medicine 1999;42:952–962.

[16] Griswold Mark A, Jakob Peter M, Heidemann Robin M, Nittka Mathias, Jellus Vladimir, Wang Jianmin, Kiefer Berthold, Haase Axel. Generalized Autocalibrating Partially Parallel Acquisitions (GRAPPA). Magnetic Resonance in Medicine 2002;47:1202–1210.

[17] Lustig Michael, Donoho David, Pauly John M. Sparse MRI: The Application of Compressed Sensing for Rapid MR Imaging. Magnetic Resonance in Medicine 2007;58:1182–1195.

[18] Boubertakh R, Prieto C, Batchelor P G, Uribe S, Atkinson D, Eggers H, Sørensen T S, Hansen M S, Razavi R S, Schaeffter T. Whole-Heart Imaging Using Undersampled Radial Phase Encoding (RPE) and Iterative Sensitivity Encoding (SENSE) Reconstruction. Magnetic Resonance in Medicine 2009;62:1331–1337.

[19] Doneva M, Eggers H, Börnert Peter. CS-SENSE or Denoised SENSE: The Influence of Irregular Sampling in l1 Regularized SENSE Reconstruction. In: Proceedings of the 20th Annual Meeting of ISMRM, Melbourne, Australia; 2012. p 2240.

[20] Cheng J Y, Zhang T, Alley M T, Lustig M, Vasanawala S S, Pauly J.M. Variable-Density Radial View-Ordering and Sampling for Time-Optimized 3D Cartesian Imaging. In: Proceedings of the ISMRM Workshop on Data Sampling and Image Reconstruction, Sedona, AZ, USA; 2013.

[21] Forman Christoph, Piccini Davide, Grimm Robert, Hutter Jana, Hornegger Joachim, Zenge Michael O. High-resolution 3D whole-heart coronary MRA: a study on the combination of data acquisition in multiple breath-holds and 1D residual respiratory motion compensation. Magnetic Resonance Materials in Physics, Biology and Medicine 2014, doi: 10.1007/s10334-013-0428-x:1–9.

[22] Prieto Claudia, Doneva Mariya, Usman Muhammad, Henningsson Markus, Greil Gerald, Schaeffter Tobias, Botnar René M. Highly efficient respiratory motion compensated free-breathing coronary mra using golden-step Cartesian acquisition. Journal of Magnetic Resonance Imaging 2014, doi: 10.1002/jmri.24602.

[23] Bhat Himanshu, Ge Lan, Nielles-Vallespin Sonia, Zuehlsdorff Sven, Li Debiao. 3D radial sampling and 3D affine transform-based respiratory motion correction technique for free-breathing whole-heart coronary MRA with 100% imaging efficiency. Magnetic Resonance in Medicine 2011;65:1269–1277.

[24] Pang Jianing, Bhat Himanshu, Sharif Behzad, Fan Zhaoyang, Thomson Louise E J, LaBounty Troy, Friedman John D, Min James, Berman Daniel S, Li Debiao. Whole-heart coronary MRA with 100% respiratory gating efficiency: Self-navigated three-dimensional retrospective image-based motion correction (TRIM). Magnetic Resonance in Medicine 2014;71:67–74.

[25] Rudin Leonid I, Osher Stanley, Fatemi Emad. Nonlinear total variation based noise removal algorithms. Physica D: Nonlinear Phenomena 1992;60:259–268.

[26] Wang Yi, Riederer Stephen J, Ehman Richard L. Respiratory Motion of the Heart: Kinematics and the Implications for the Spatial Resolution in Coronary Imaging. Magnetic Resonance in Medicine 1995;33:713–719.

[27] Nocedal Jorge. Updating Quasi-Newton Matrices With Limited Storage. Mathematics of Computation 1980;35:773–782.

[28] Li D, Carr J C, Shea S M, Zheng J, Deshpande V S, Wielopolski P A, Finn J P. Coronary Arteries: Magnetization-prepared Contrast-enhanced Three-dimensional Volume-Targeted Breath-hold MR Angiography. Radiology 2001;219:270–277.

[29] Piccini Davide, Monney Pierre, Sierro Christophe, Coppo Simone, Bonanno Gabriele, van Heeswijk Ruud B, Chaptinel Jérôme, Vincenti Gabriella, de Blois Jonathan, Koestner Simon C, Rutz Tobias, Littmann Arne, Zenge Michael O, Schwitter Juerg, Stuber Matthias. Respiratory Self-navigated Postcontrast Whole-Heart Coronary MR Angiography: Initial Experience in Patients. Radiology 2014;270:378–386.

[30] Akçakaya Mehmet, Basha Tamer A, Chan Raymond H, Rayatzadeh Hussein, Kissinger Kraig V, Goddu Beth, Goepfert Lois A, Manning Warren J, Nezafat Reza. Accelerated Contrast-Enhanced Whole-Heart Coronary MRI Using Low-Dimensional-Structure Self-Learning and Thresholding. Magnetic Resonance in Medicine 2012;67:1434–1443.

[31] Batchelor P G, Atkinson D, Irarrazaval P, Hill D L G, Hajnal J, Larkman D. Matrix Description of General Motion Correction Applied to Multishot Images. Magnetic Resonance in Medicine 2005;54:1273–1280.

[32] Odille Freddy, Vuissoz Pierre-André, Marie Pierre-Yves, Felblinger Jacques. Generalized Reconstruction by Inversion of Coupled Systems (GRICS) Applied to Free-Breathing MRI. Magnetic Resonance in Medicine 2008;60:146–157.

[33] Schmidt Johannes F M, Buehrer Martin, Boesiger Peter, Kozerke Sebastian. Non-rigid Retrospective Respiratory Motion Correction in Whole-Heart Coronary MRA. Magnetic Resonance in Medicine 2011;66:1541–1549.

[34] Lustig M, Santos J.M., Donoho D.L. k-t SPARSE: High frame rate dynamic MRI exploiting spatio-temporal sparsity. In: Proceedings of the 13th Annual Meeting of ISMRM, Seattle, WA, USA; 2006. p 2420.

[35] Otazo Ricardo, Candes Emmanuel, Sodickson Daniel K. Low-Rank Plus Sparse Matrix Decomposition for Accelerated Dynamic MRI with Separation of Background and Dynamic Components. Magnetic Resonance in Medicine 2014, doi: 10.1002/mrm.25240:1–12.

[36] Zhang Tao, Pauly John M, Levesque Ives R. Accelerating parameter mapping with a locally low rank constraint. Magnetic Resonance in Medicine 2014, doi: 10.1002/mrm.25161.

FIGURE LEGEND

Figure 1: Block diagram illustrating the workflow of the respiratory motion detection: a) A series of SI projections are plotted in temporal order. Target segments for motion detection are identified in the first SI projection. Two segments are exemplarily highlighted with a red box. b) The offsets for all subsequent SI projections are detected using the self-navigation principle and plotted for each segment. c) Then, the SI projections are resorted according to the detected offsets. The segment corresponding to the lowest signal variation in the resorted SI projections provides the best performance to describe the respiratory pattern.

Figure 2: A series of 50 SI projections, acquired in the first 50 consecutive heartbeats in the experiment with volunteer 5 is representatively displayed (left) as acquired and (right) after sorting with respect to the detected offsets. The selected interval of the respiratory motion detection is highlighted with a red line. The offsets were detected using cross-correlation with respect to this interval.

Figure 3: For volunteer 5, a 2D histogram visualizes the number of occurrences of all pairs of values from the navigator signal and the detected offset of the proposed method with colors in the background. While red dots highlight all available pairs of values, linear regression is represented by the black line. The resolution in the SI projection is given by the acquired voxel size, here 1.05 mm, whereas that of the navigator was 1.0 mm. For this specific volunteer, both signals had a correlation of 0.96 and the slope of the linear regression was 0.99.

Figure 4: Reformatted images showing the RCA of the same volunteer at the identical position. The volumes were reconstructed with the proposed weighted iterative reconstruction utilizing different weighting functions. For "Gaussian", the standard deviation of the weighting kernel was set to A) 1.25 pixels, B) 2.75 pixels, and C) 3.75 pixels, which resulted in an estimated vessel sharpness of $0.385 \pm 0.076\,\mathrm{mm}^{-1}$, $0.375 \pm 0.065\,\mathrm{mm}^{-1}$, and $0.343 \pm 0.029\,\mathrm{mm}^{-1}$, respectively. For "Box", the size of the acceptance window was set to A) ± 2.5 pixels, B) ± 5.5 pixels, and C) ± 7.5 pixels. In the resulting volumes, vessel sharpness was estimated with $0.369 \pm 0.083\,\mathrm{mm}^{-1}$, $0.306 \pm 0.044\,\mathrm{mm}^{-1}$, and $0.288 \pm 0.032\,\mathrm{mm}^{-1}$, respectively.

Figure 5: Box plot for comparison of image quality after weighted iterative reconstruction with different weighting functions. Vessel sharpness was estimated in the LAD (top) and RCA (bottom) in the reconstructed volumes obtained from 14 volunteers.

Figure 6: Reformatted images of two selected volunteers showing the LAD and RCA. Reconstructed volumes without compensation suffer from artifacts due to respiratory motion during the free-breathing acquisition ("Uncompensated"), while the proposed method was able to improve the vessel sharpness significantly by suppressing motion artifacts in image reconstruction ("Weighting"). Additionally, reconstructed volumes of the weighted approach show a comparable vessel length and sharpness to the navigator-gated reference acquisition.

Figure 7: Box plot for comparison of image quality parameters estimated in vessel sharpness (top), length (middle), and visual scores (bottom) obtained from the reconstructed volumes of 14 volunteers. Data was acquired during free-breathing and reconstructed with and without weighted iterative reconstruction. The resulting image quality was compared to a navigator-gated reference acquisition.

Figure 8: For two volunteers, the distribution of the respiratory offsets as detected in the SI projections is illustrated using histograms. The acquired data was reconstructed using weighted iterative reconstruction based on the plotted weighting function. Both volumes were reconstructed with data from 262 (top row) and 252 (bottom row) heartbeats that were weighted greater than 0.05 in the weighting matrix. Axial and sagittal slices of the resulting volumes are depicted next to the corresponding histograms. The corresponding navigator-gated reference acquisition of both volunteers required 6.9 min and 6.6 min, respectively.

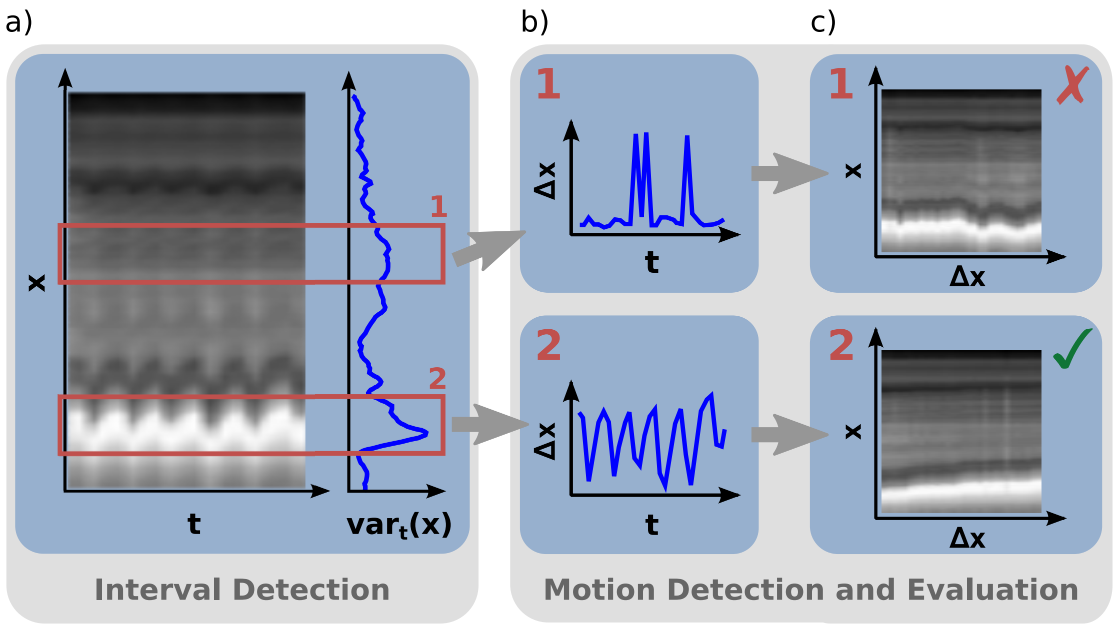

Figure 1: Block diagram illustrating the workflow of the respiratory motion detection: a) A series of SI projections are plotted in temporal order. Target segments for motion detection are identified in the first SI projection. Two segments are exemplarily highlighted with a red box. b) The offsets for all subsequent SI projections are detected using the self-navigation principle and plotted for each segment. c) Then, the SI projections are resorted according to the detected offsets. The segment corresponding to the lowest signal variation in the resorted SI projections provides the best performance to describe the respiratory pattern.

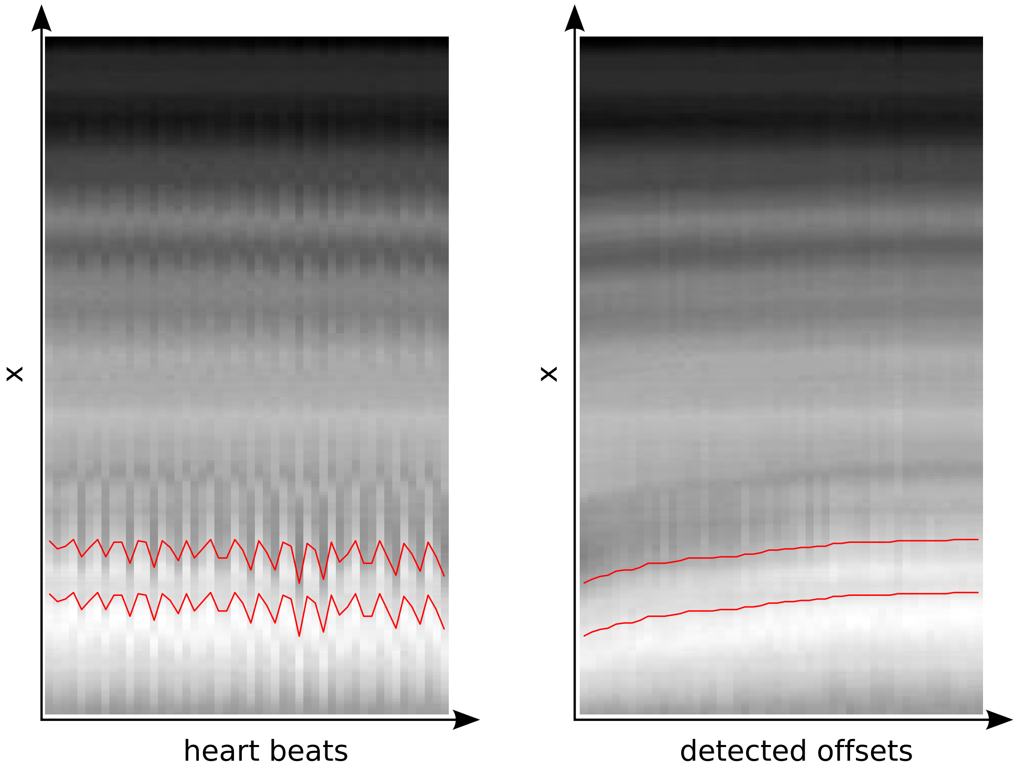

Figure 2: A series of 50 SI projections, acquired in the first 50 consecutive heartbeats in the experiment with volunteer 5 is representatively displayed (left) as acquired and (right) after sorting with respect to the detected offsets. The selected interval of the respiratory motion detection is highlighted with a red line. The offsets were detected using cross-correlation with respect to this interval.

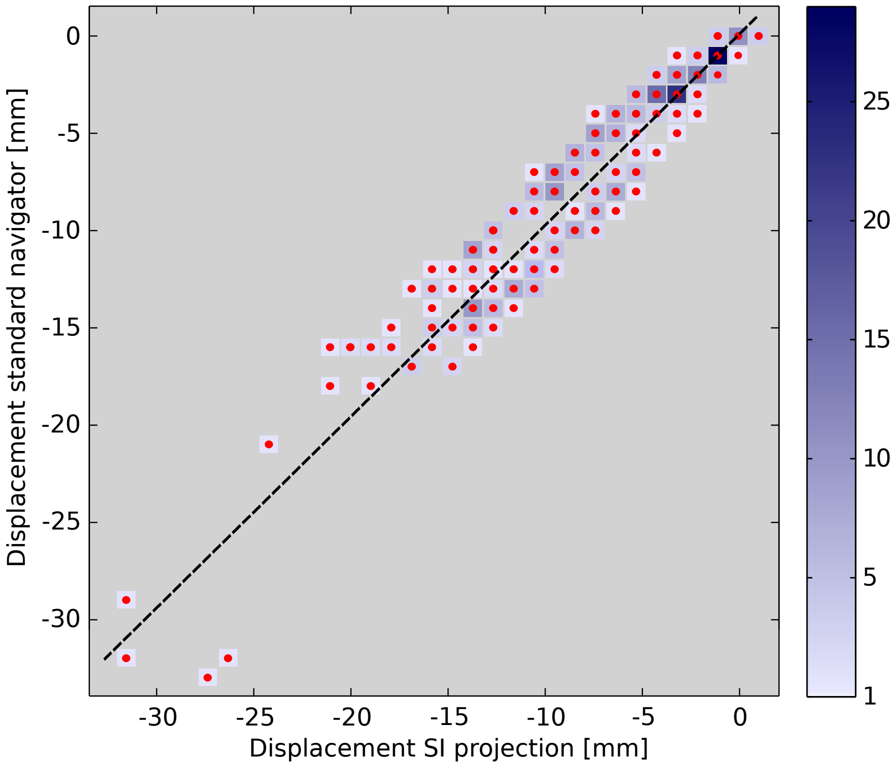

Figure 3: For volunteer 5, a 2D histogram visualizes the number of occurrences of all pairs of values from the navigator signal and the detected offset of the proposed method with colors in the background. While red dots highlight all available pairs of values, linear regression is represented by the black line. The resolution in the SI projection is given by the acquired voxel size, here 1.05 mm, whereas that of the navigator was 1.0 mm. For this specific volunteer, both signals had a correlation of 0.96 and the slope of the linear regression was 0.99.

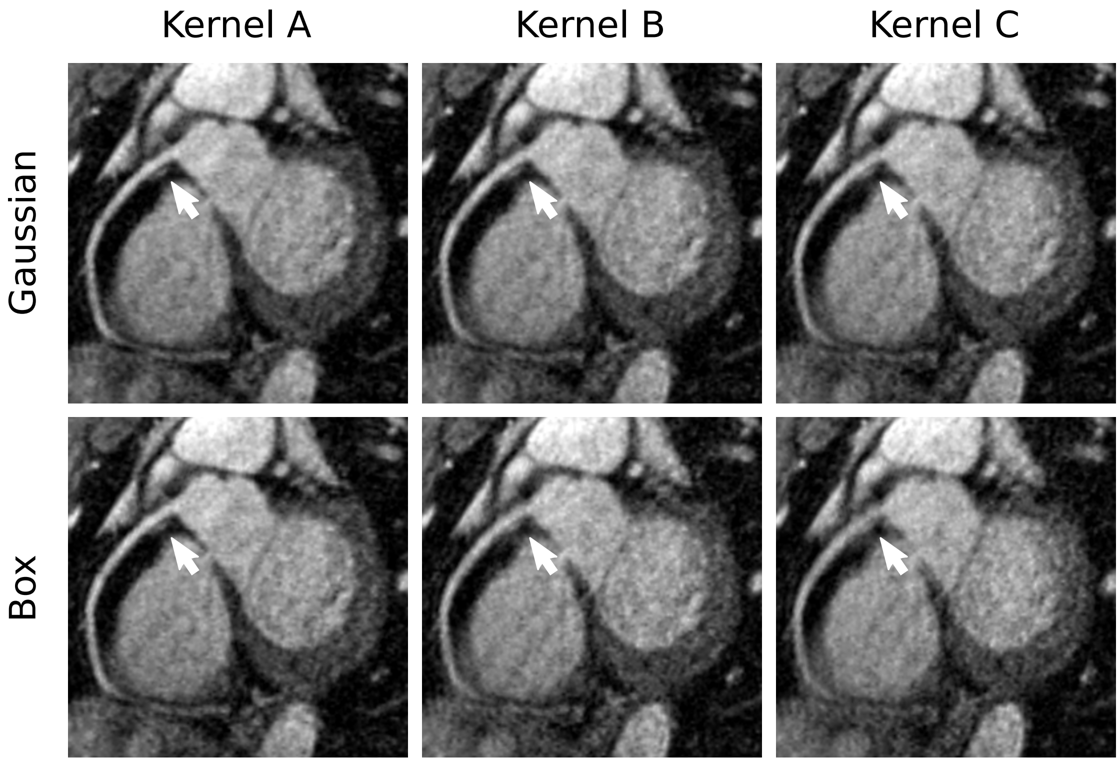

Figure 4: Reformatted images showing the RCA of the same volunteer at the identical position. The volumes were reconstructed with the proposed weighted iterative reconstruction utilizing different weighting functions. For "Gaussian", the standard deviation of the weighting kernel was set to A) 1.25 pixels, B) 2.75 pixels, and C) 3.75 pixels, which resulted in an estimated vessel sharpness of $0.385 \pm 0.076\,\mathrm{mm}^{-1}$, $0.375 \pm 0.065\,\mathrm{mm}^{-1}$, and $0.343 \pm 0.029\,\mathrm{mm}^{-1}$, respectively. For "Box", the size of the acceptance window was set to A) ± 2.5 pixels, B) ± 5.5 pixels, and C) ± 7.5 pixels. In the resulting volumes, vessel sharpness was estimated with $0.369 \pm 0.083\,\mathrm{mm}^{-1}$, $0.306 \pm 0.044\,\mathrm{mm}^{-1}$, and $0.288 \pm 0.032\,\mathrm{mm}^{-1}$, respectively.

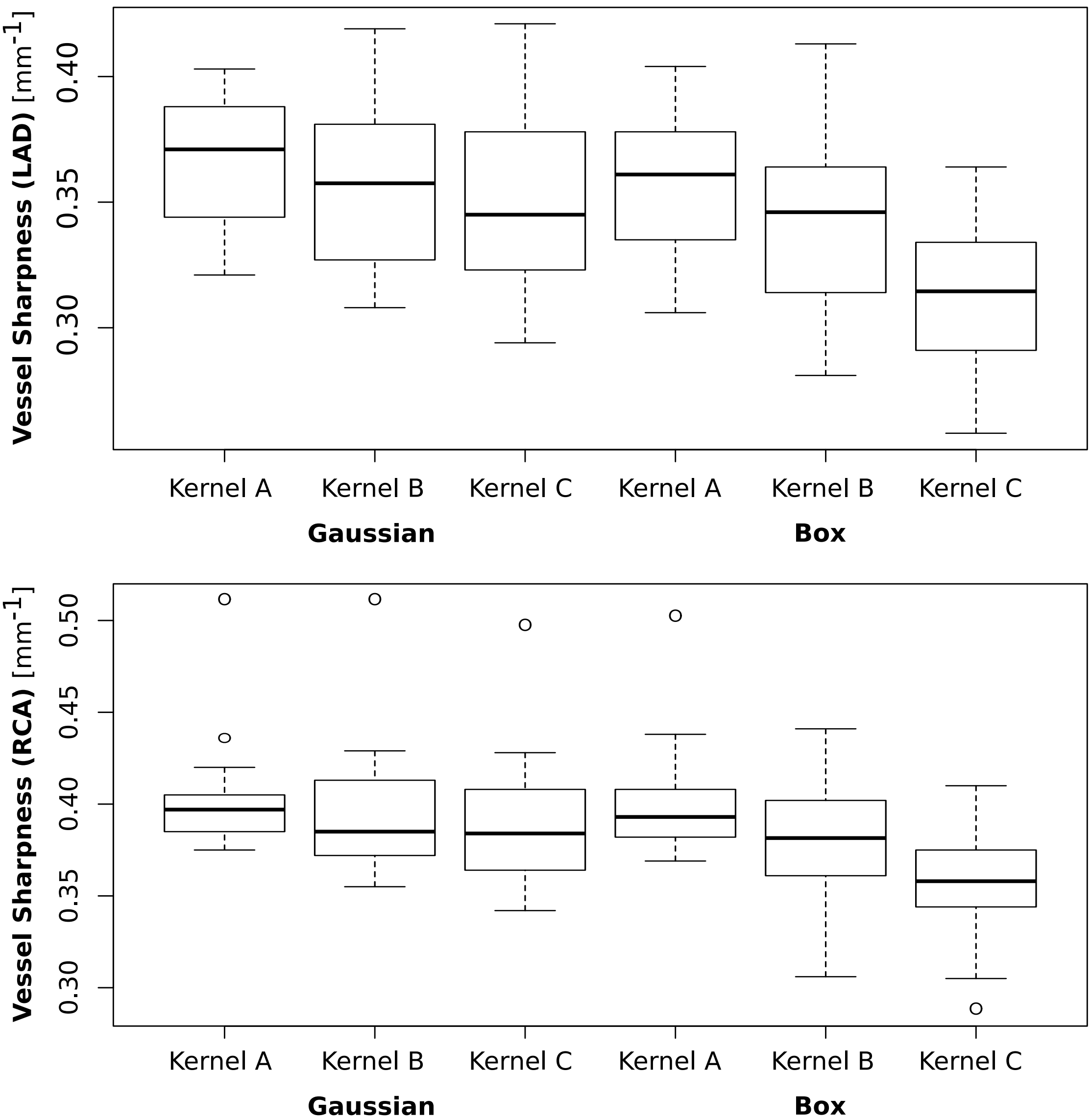

Figure 5: Box plot for comparison of image quality after weighted iterative reconstruction with different weighting functions. Vessel sharpness was estimated in the LAD (top) and RCA (bottom) in the reconstructed volumes obtained from 14 volunteers.

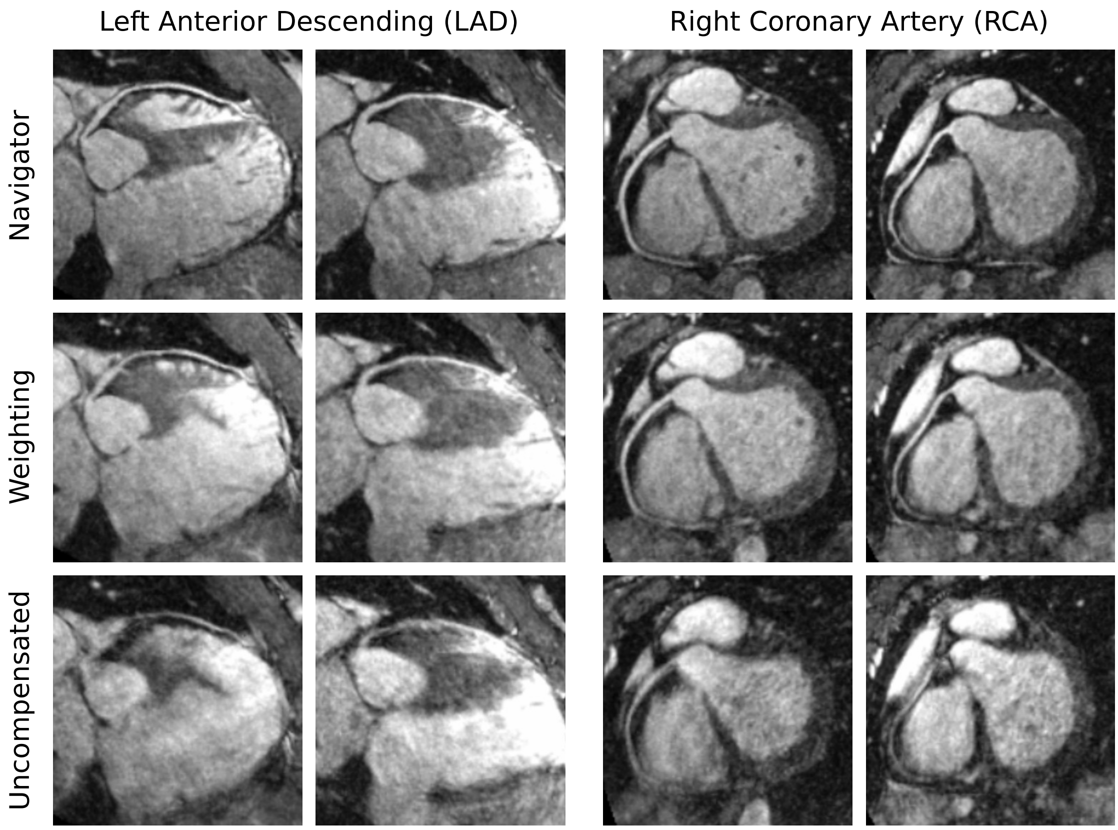

Figure 6: Reformatted images of two selected volunteers showing the LAD and RCA. Reconstructed volumes without compensation suffer from artifacts due to respiratory motion during the free-breathing acquisition ("Uncompensated"), while the proposed method was able to improve the vessel sharpness significantly by suppressing motion artifacts in image reconstruction ("Weighting"). Additionally, reconstructed volumes of the weighted approach show a comparable vessel length and sharpness to the navigator-gated reference acquisition.

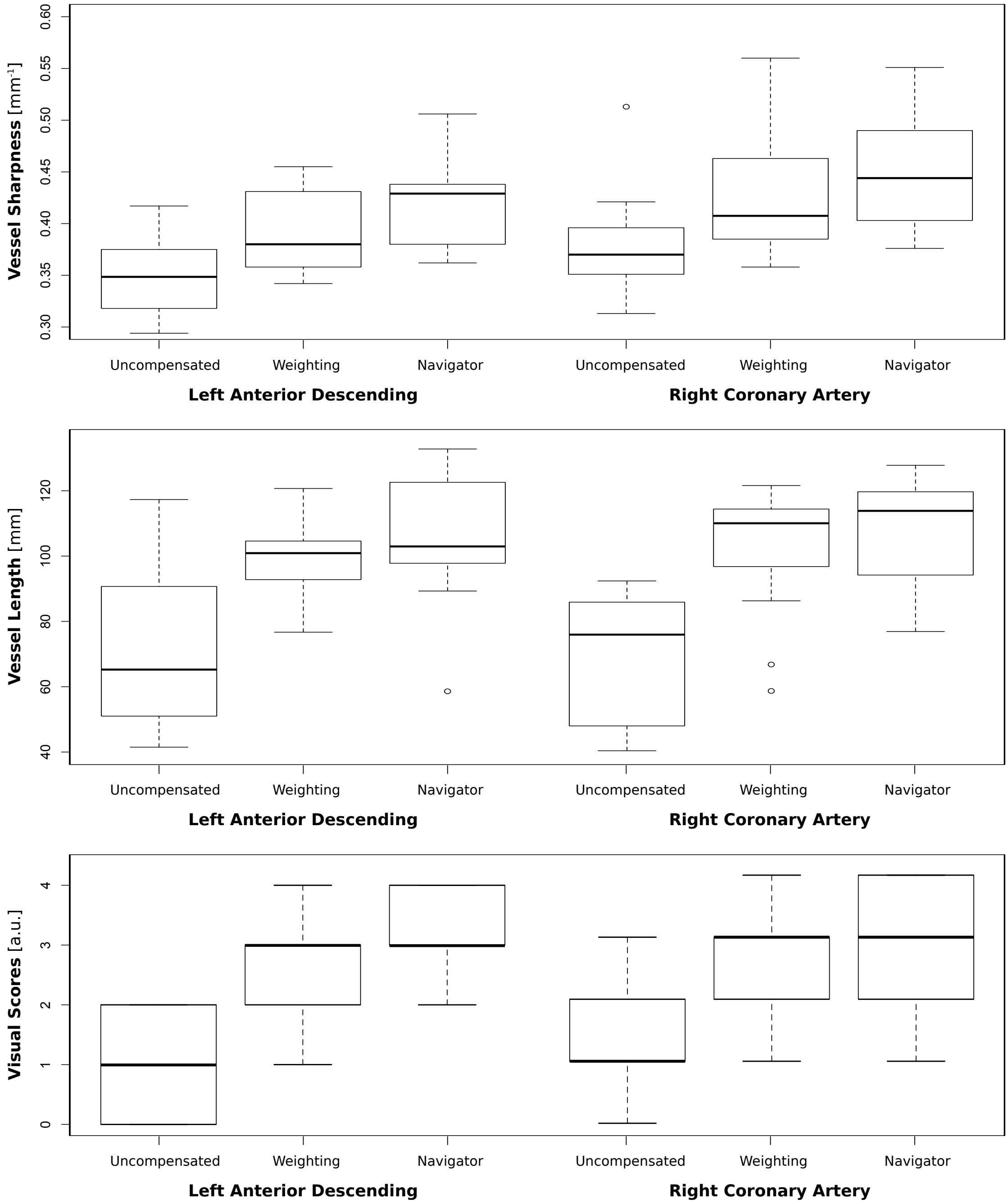

Figure 7: Box plot for comparison of image quality parameters estimated in vessel sharpness (top), length (middle), and visual scores (bottom) obtained from the reconstructed volumes of 14 volunteers. Data was acquired during free-breathing and reconstructed with and without weighted iterative reconstruction. The resulting image quality was compared to a navigator-gated reference acquisition.

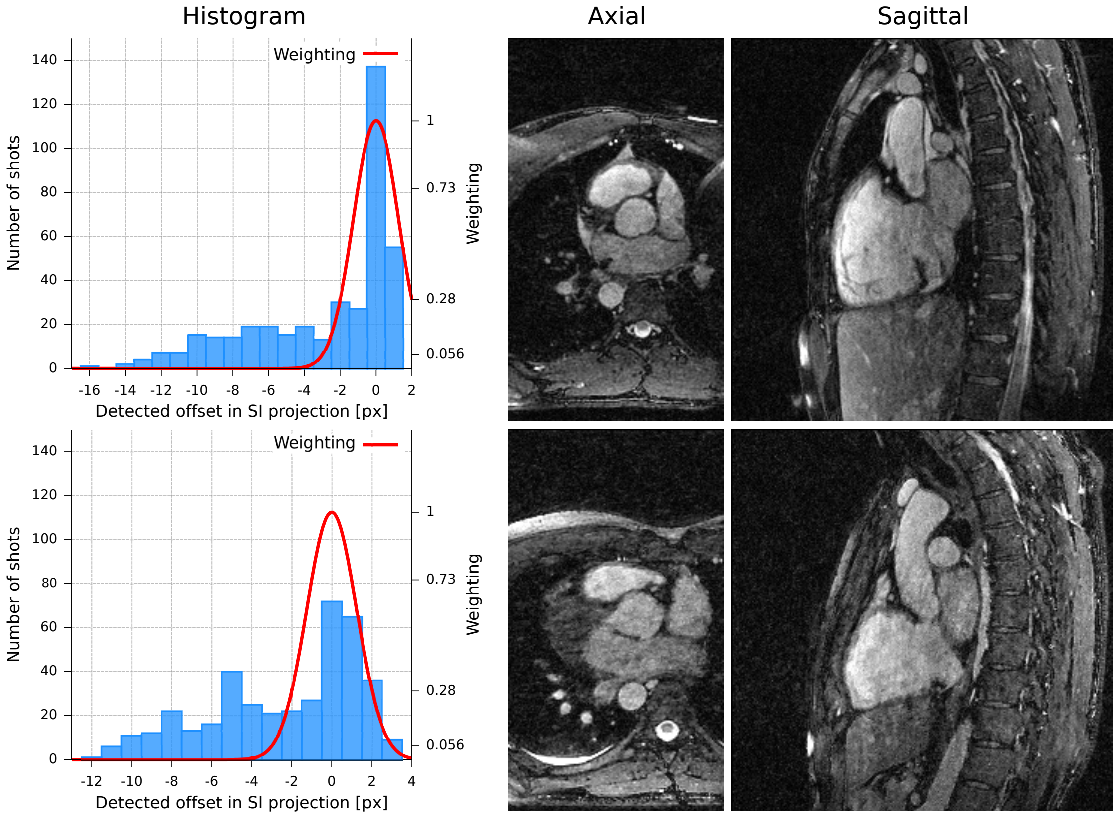

Figure 8: For two volunteers, the distribution of the respiratory offsets as detected in the SI projections is illustrated using histograms. The acquired data was reconstructed using weighted iterative reconstruction based on the plotted weighting function. Both volumes were reconstructed with data from 262 (top row) and 252 (bottom row) heartbeats that were weighted greater than 0.05 in the weighting matrix. Axial and sagittal slices of the resulting volumes are depicted next to the corresponding histograms. The corresponding navigator-gated reference acquisition of both volunteers required 6.9 min and 6.6 min, respectively.